SAND2000-0606J

Gravity destabilized non-wetting phase invasion in macro-heterogeneous porous media: Near pore scale macro modified invasion percolation simulation of experiments

Robert J Glass, Stephen Conrad, and Lane Yarrington
Flow Visualization and Processes Laboratory
Sandia National Laboratories, Albuquerque, NM

November 15, 1999

Abstract

We reconceptualize 'macro' modified invasion percolation (MMIP) at the near pore (NP) scale and apply it to simulate the non-wetting phase invasion experiments of Glass et al [in review] conducted in macro-heterogeneous porous media. For experiments where viscous forces were non-negligible, we redefine the total pore filling pressure to include viscous losses within the invading phase as well as the viscous influence to decrease randomness imposed by capillary forces at the front. NP-MMIP exhibits the complex invasion order seen experimentally with characteristic alternations between periods of gravity stabilized and destabilized invasion growth controlled by capillary barriers. The breaching of these barriers and subsequent pore scale fingering of the non-wetting phase is represented extremely well as is the saturation field evolution, and total volume invaded.

DISCLAIMER

1. Introduction

Recent experiments presented in Glass et al. [in review] henceforth referred to as GC&P, have demonstrated the complexity of the gravity destabilized non-wetting invasion process in macro-heterogeneous porous media and suggested the difficulty of attempting simulation using standard porous continuum approaches. These experiments show a characteristic alternation between gravity stabilized and destabilized invasion growth controlled by the sequential capillary barriers (CBs) within the heterogeneous field. The final non-wetting invasion structure existed as a set of macroscopic pools connected by pore scale fingers. Viscous forces were shown to increase the number of fingers, their width, and the height of pools above CBs. The experiments also documented unsteady pulsation behind the invasion front, however, the pulsation did not significantly influence the maximum extent of the invasion structure.

In an accompanying analysis, GC&P also developed length scales that describe pool height, finger width and pulsation. Each of these length scales required conceptualization at the pore scale to predict experimental behavior. To avoid the problems of porous continuum simulation, a 'structural' growth model was proposed at the macro scale that would assemble these length scales to build the non-wetting phase migration pathway directly, its geometry of fingers and pools, and the locations of pulsation within a complex heterogeneous formation. Such an approach is underpinned by the physics of the pore scale behavior and indeed is a variant of 'Macro' or 'Upscaled' Modified Invasion Percolation (MMIP) developed and applied originally by [Glass et al. 1993, 1995] to the migration problem.

The development of such a MMIP approach is in its infancy compared to conventional porous continuum conceptualizations of reality. Here we continue to lay a foundation for MMIP by first reconceptualizing it generally in a form that encompasses the near pore (NP) scale and then comparing NP-MMIP simulations to the laboratory experiments presented in GC&P. Our initial NP-MMIP simulations of the experiments show several discrepancies which lead to modifications for small capillary property mismatches and the inclusion of viscous effects. Once these modifications are accomplished, we find that NP-MMIP can model the complex experimental invasion sequence and saturation field evolution exceptionally well, both when viscous forces are negligible, and when they are not.

2. MMIP and NP-MMIP model conceptualization

MMIP bases its properties for spanning a grid-block of porous media (the macro-scale) on the smaller scale pore network behavior seen in standard Invasion Percolation (IP) simulations [e.g., Wilkinson and Willemsen, 1983] and pore network micro-model experiments [e.g., Lenormand and Zarcone, 1985]. We note that this approach has also been suggested by Kueper and McWorter [1992] and Ioannidis et al. [1996] for gravity stabilized conditions. In isotropic, random pore networks with no spatial correlation, as an invading fluid displaces a defending fluid, a threshold radius is achieved after which the network is spanned, or 'percolates,' in all directions. The radius at this percolation threshold is used in the macro model to represent a 'spanning' radius, R, for the block. The capillary pressure required to achieve the spanning radius is given by:

$$P_c = \frac{-2\sigma\cos(\alpha)}{R} \tag{1}$$

where σ is the interfacial tension, and α is the effective contact angle within the fluid/fluid/solid system (α between 0 and 90 degrees for wetting and 90 and 180 for non-wetting invasion). Gravity forces are represented by the hydrostatic pressure:

$$P_g = \Delta\rho g z \tag{2}$$

where $\Delta\rho$ is the density difference between the two fluids ($\rho_{defender}$-$\rho_{invader}$), g is the acceleration due to gravity, and z is the distance into the network positive in the direction of g. The total invasion pressure for a block is simply given by:

$$P_t = \frac{-2\sigma\cos(\alpha)}{R} + \Delta\rho g z \tag{3}$$

Implementation of MMIP requires the problem domain to be discretized into a grid (2 or 3D) with a chosen connectivity and R values assigned to each grid block. An IP algorithm is then applied on the P_t field to determine the growth pattern in time as invading fluid is added at the injection point. An IP algorithm simply selects the block connected to the growing cluster that has the lowest total invasion pressure as calculated using equation (3) and invades it. When a block is invaded, the list of blocks connected to the growing cluster is modified, sorted, the next block with the lowest invasion pressure selected, invaded, and so on.

Because in MMIP we do not consider the details of individual 'throats' and 'pores' but rather the behavior of a sub-network of these features, R represents the critical 'throat' or critical 'pore' within the block for non-wetting or wetting fluid invasion, respectively. We can also apply this conceptual model at the 'near pore scale' (NP) where a block contains a small void space 'network' that is characterized by local spanning radii for wetting and non-wetting invasion. For this NP-MMIP conceptualization, the characteristic R distribution is obtained directly from measured primary drainage, capillary pressure-saturation curves for the material of interest. Normalizing saturation by $(1 - S_{wr})$, where S_{wr} is the wetting fluid residual value, and then transforming capillary pressure to effective R using equation (1) yields a cumulative probability distribution function (CDF) for R that characterizes the material of interest. S_{wr} for the near pore scale represents wetting phase that is contained in films, pendular rings between grains, and trapped pores within the void space. At this scale, trapping of the defending phase could be considered directly when a

block is surrounded by other blocks. In our application here, we will not consider such block-scale trapping directly but represent this process in the residual value.

MMIP has many advantages over traditional forms of IP where the conceptual model is tied to balls and sticks or even more complicated 'throat' and 'pore' geometries (e.g., Reeves et al. 1996). Such geometries are difficult to justify topologically in granular porous media and can actually lead to a divergence between model results and data. Instead, we make use of easily measured pressure-saturation curves directly with an appropriate volume averaged conceptual model. This also contrasts with the standard continuum approach based on an REV; at the near pore scale, we do not require that the property be 'uniform' and instead capture its stochastic nature within the R field.

Application of NP-MMIP requires discretizing the problem into a network of blocks and specifying a connectivity between blocks. For simplicity we work with discretizations that divide the domain into a grid of cubes. At the NP scale, the mean grain size is representative of the average spacing between pores and so represents a reasonable lower limit for grid block size. The mean grain size may vary from unit to unit. Results are relatively insensitive to the scale of discretization above the mean grain size until the block size becomes on order of the variation in capillary potential within a unit. When this happens, gravity begins to artificially overwhelm capillary forces within a particular unit. This issue requires additional study with respect to upscaling but is less important in our current NP conceptualization and application here.

Connectivity influences the invasion structure by controlling the subset of blocks that are available for filling. The larger the connectivity, the larger this distribution and the higher the probability of finding blocks with a lower spanning pressure. In this study our choice of a cubic grid constrains us to connectivities of 4 (orthogonal) and 8 (orthogonal plus diagonal) in 2D and 6 (orthogonal) and 26 (orthogonal plus diagonal) in 3D. Within a gravity field, the connectivity also influences the relative weighting of horizontal to vertical invasion. Orienting down the gravitational potential gradient, a connectivity of: 4 in 2D has 2 horizontal blocks, 1 downstream, 1 upstream; 8 in 2D has 2 horizontal blocks, 3 downstream, 3 upstream; 6 in 3D has 4 horizontal blocks, 1 downstream, 1 upstream; and 26 in 3D has 8 horizontal blocks, 9 downstream, 9 upstream. This connectivity biases growth within a gravity field because greater/lesser access to pores in a given direction will lead to a higher/lower probability of growth in that direction. Thus, slightly narrower fingers are simulated in 3D networks and when both orthogonal and diagonal blocks are accessible.

Additional processes that influence P_t can be easily added within the NP-MMIP model. First and second order viscous effects will be discussed later in comparison to experiment. Other modifications such as the influence of macroscopic interfacial curvature, local saturation dependent viscous forces, or variability in time and space of the contact angle can also be incorporated as can simultaneous drainage and wetting such as seen in experiments that exhibit pulsation. However, we will not discuss these additional modifications further here.

3. Comparison of NP-MMIP to experiment:

Experiments reported in GC&P were designed and conducted within a thin (1 cm) but extensive (26 cm wide, 60 cm tall) sand chamber filled with translucent sands such that saturation and invasion order integrated over the thickness of the chamber could be monitored in time using quantitative light transmission visualization techniques. The heterogeneous sand structure (hetero-structure) was composed of a series of capillary barriers (CBs) reminiscent of fluvial channel lag cut-and-fill architecture created with three sand units: coarse, medium, and fine (sand properties given in Table 1). Gravity destabilized, non-wetting phase invasion experiments were conducted where the interfacial tension, density difference and viscosity were varied between two fluid/fluid systems: CO_2/water and TCE/water (fluid properties given in Table 2). The non-wetting fluid was injected into the water saturated hetero-structure near the middle of one end and the invasion process was recorded in a series of high resolution digital images (taken every ~0.33 ml of injected fluid) until the non-wetting phase reached the far side of the chamber. Digital images were processed to provide quantitative saturation fields (pixel size 0.4495 mm by 0.4495 mm across the entire experimental field) that clearly showed the pore scale nature of the invasion process.

Here we consider only the CO_2 and TCE experiments that were conducted in the same sand pack (the 'primary' hetero-structure, Figure 1a of GC&P) where CO_2 was initially injected from below, dissolved away, the chamber inverted, and finally TCE injected from above. Because flow rates for these two invasion experiments were nearly the same (1.2 ml/min. for CO_2 and 0.90 ml/min. for TCE), viscous forces relative to capillary and gravity forces were substantially different because of the ~ 40 times greater viscosity of TCE relative to CO_2. Analysis of results presented in GC&P suggested that while viscous forces were negligible for the CO_2 system, they were non-negligible for the TCE/water experiments. Thus, by considering these experiments conducted in the same hetero-structure, we can assess NP-MMIP where the development in Section 2 applies and then consider modifications to the model for viscous effects in context of the data.

In the following, we first describe our problem definition and simulation processing procedures. We then present a set of initial simulations and compare to the experimental results. We follow with a set of modified simulations that first correct for capillary property discrepancies and then include first and second order viscous influences. Finally, we evaluate the saturation fields simulated by NP-MIP in light of the experiments.

3.1 Problem definition and simulation processing:

We translated the experimental hetero-structure into a field of effective spanning radius values by first dividing the digital image of the sand pack (580x1236 pixels) into the individual sand types using pixel intensity (the coarser the unit, the more light passes). Edges of units were then resolved by eye where digital methods failed due to light scatter. The image was then re-scaled to yield the template 'unit' network with block size equal to the mean grain size of the coarse unit (240x511 pixels, 0.1087^2 cm^2/pixel). For 3D networks, the 2D unit field was 'extruded' to the thickness of the experiment (9 blocks). Each block in the resulting unit network was then assigned an R value using CDFs built from the measured primary drainage pressure-saturation curves for each unit as described above. Within each unit, we assumed no spatial correlation when assigning R.

The hetero-structure and a representative pore radius field are shown in Figure 1 a and b. As a simple check on our NP-MMIP formulation and assignment method for R field

distributions, we conducted gravity stabilized air invasion simulations of the experiments used to measure the primary drainage pressure-saturation curves. Comparison of the final equilibrium (hydrostatic) profiles are shown in Figure 1 c. As we would expect, the results are nearly identical. Small differences occur only near the non-wetting entry value where simulations are slightly more abrupt than the experimental data suggests.

To compare with experimental invasion data, composite 2D order images are compiled by tracking the first invasion at a location across the thickness of the 3D network just as our image analysis of the sequential saturation fields did to develop similar order images from the experimental data. Additionally, 2D saturation fields are calculated from the 3D network results by averaging across the thickness of the network. Images in all figures are oriented such that flow is in the same direction to facilitate comparison, i.e., the CO_2 invasion is rotated 180 degrees with gravity now acting upward in the image. Invaded volumes were calculated by multiplying the volume of invaded blocks by the product of $(1-S_{wr})$ and the porosity, both taken for the coarse sand as 0.83 and 0.35, respectively.

3.2 Initial simulations:

A full suite of CO_2 and TCE invasion simulations were conducted on both 2D (connectivity 4 and 8) and 3D (connectivity 6 and 26) networks using 10 different realizations of each R field. Comparison across the different realizations shows some variability with slight differences in pool height, finger location, and final invaded volume at breakthrough. Additionally, directional bias inherent in the choice of network dimensionality and connectivity slightly influences the details of finger structure and saturation. For the sake of brevity, we choose to present in the figures below only the 3D orthogonal results for a single R field realization as they most closely match the data.

Composite order images shown in Figure 2 show a strong qualitative similarity to the experimental images. At breakthrough, the field is composed of a series of macroscopic pools connected by pore scale fingers. The breaching of CBs also is pore scale as we found in the experiments. However, we see many quantitative differences between simulations and experiment, e.g., pool height and finger width, which lead to significant errors in the total volume invaded at breakthrough (see Table 3). Colors in the figure represent invasion order and when they match between images, the sequence in time matches as well. Most of the volume and invasion sequence error is found associated with the pools. Additionally, comparison of TCE to CO_2 simulations shows the TCE invasion pathway to have pools of lower height and connecting fingers that are slightly narrower, exactly opposite of what we found experimentally.

There are two main causes for the discrepancies between our initial simulations and experiments. First, there is a mismatch between the capillary properties measured for the medium sand units and those composing the CB units within the heterogeneous sand slab. This causes pool height above CBs for CO_2 invasion to be over predicted by ~30%. We also see a slight mismatch of capillary properties at the narrowest point of the coarse sand run in the middle of the chamber. Here two units of the medium sand came very near to each other and close inspection showed that some of the medium sand mixed with the coarse thus reducing the local R values at the restriction point. The second cause is due to the neglect of viscous forces in our model formulation. Our simulations yield pool heights above CBs that are lower for TCE than for CO_2, and finger widths that are slightly narrower, consistent with an assumption of negligible viscous forces. However, as we showed in GC&P, viscous forces are not negligible for the TCE invasions and so experimental pool height and finger width is actually greater for TCE than CO_2. Additionally, the breaching of CBs occurs at only a single point while we found multiple

fingers to span the CB for TCE, also an influence of increased viscous forces. To better simulate the experiments, we now consider several modifications that address these property and viscous discrepancies.

3.3 R field modifications:

The increase in the pore sizes within the medium sand CBs is easily captured by scaling its R distribution. When viscous forces are negligible, analysis in GC&P found a factor of 1.2 was required to fit the experimental pool heights for the CO_2 invasion. In order to capture the additional influence of the coarse and medium sand mixing at the restriction within the long coarse sand run in the middle of the chamber, we also scaled the R's in this region by a factor of 0.95. Results shown in Figure 3 a show that we now simulate pool heights very well for CO_2 including that above the middle restriction. Additionally, the invasion order is now nearly identical to the experiment as is the CO_2 volume at breakthrough (see Table 3). For TCE, shown in Figure 3 b, pool height is further depressed with correspondingly greater discrepancies for invasion order and TCE volume.

3.4 Viscous force modifications:

To fully treat the TCE invasion we must include viscous forces within the NP-MMIP model. Two approaches have been suggested recently in the literature. Xu et al. [1998] consider a viscous influence proportional to the capillary number and viscosity ratio. Ewing and Berkowitz [1998] make use of two statistical relations that modify the IP search algorithm to first cause the filling in of the network behind the front and second, initiate independent gravity-driven fingers. While each of these approaches are instructive, neither is able to fully explain the experimental behavior in GC&P. Here we propose an alternative approach that includes first order effects similar to Xu et al. [1998] and then second order effects similar to Ewing and Berkowitz [1998]. For each of these, our formulations are guided by data and depart somewhat from the previous theoretical development.

Based on experimental results, in GC&P we found that in every case considered (e.g., finger width, finger pulsation, maximum pool height and pool pulsation), incorporating viscous forces within the invading phase alone with appropriate recognition of the conducting pore scale geometry allowed us to predict experimental behavior closely. Viscous forces increase the pressure within the invading phase from the invading front back to the source. Assuming the defending phase's pressure is uninfluenced, the P_t required to span a block decreases back along this path as well. Thus we propose the total block spanning pressure can be modified to include first order viscous forces as:

$$P_t = \frac{-2\sigma\cos(\alpha)}{R} + \Delta\rho g z - \frac{Q\mu L}{k k_r A} \qquad (4)$$

where Q is the applied flow rate, μ is the viscosity of the invading fluid, L is the distance back along the flow path from the invasion front to the block of interest, k and k_r are the intrinsic and relative permeability of the material along the path, and A is the cross-sectional area of the conducting pathway normal to the local flux. As discussed in GC&P, for fingers, A corresponds to the conductive finger backbone, while within the pools, A increases to the full cross-sectional area normal to the flow direction. Full implementation of (4) requires that A, L, and k_r be determined locally as the invasion progresses, a complicated and computationally expensive task outside the scope of this paper. Here we are interested in a simplified effective application that is accomplished within the context of

the current NP-MMIP model. Therefore, we focus on the critical situations in the experiment where viscous forces are non-negligible and incorporate them in an effective sense thus avoiding local transient modification of P_t.

Our primary viscous discrepancy occurs at CBs where viscous forces primarily act vertically. For this one dimensional view, $L=z_f-z$ where z_f is the position of the front. Taking effective values for k, k_r, and A (subscript e) that apply to the pool/CB system we may write:

$$P_t = \frac{-2\sigma\cos(\alpha)}{R} + \left[\Delta\rho g + \frac{Q\mu}{k_e k_{re} A_e}\right] z - \frac{Q\mu}{k_e k_{re} A_e} z_f \qquad (5)$$

Recognizing that the final term is a constant throughout the invading phase at a given growth step, it does not influence the choice of which block to invade. Thus, in this first order formulation, we see that the viscous term simply adds to the gravitational term and can be incorporated globally within NP-MMIP. To approximate the effective viscous factor, we consider the increase in pool height above CBs. Using the relation for the maximum pool height developed in the scale analysis of GC&P (i.e., their equation 5), simplifying it to an effective system composed of a pool and barrier with single effective k, k_r, and A, denoting the value of the pool height with no viscous influence as h_{pcap} and that with viscous influence as h_{pvis}, and solving for the viscous factor yields:

$$\frac{Q\mu}{k_e k_{re} A_e} \sim \Delta\rho g\left[1 - \frac{h_{pcap}}{h_{pvis}}\right] \qquad (6)$$

The ratio of h_{pcap} to h_{pvis} for the medium-coarse sand CB in the TCE experiments was found to be 0.41. Applying (5) globally using this viscous factor will also slightly increase finger width. It will not, however, influence horizontal paths. Non-negligible viscous forces along a primarily horizontal path is observed experimentally within the pool above CB4 where the pool is higher near the entry point on the right than on the far left. We can treat this discrepancy regionally by including a horizontal component of the viscous pressure using measured values of k for the coarse unit (k_r=1) and taking A_e to be the height of the pool. A simulation on the modified R distribution field that includes both the global vertical viscous component and the horizontal component in this pool is shown in Figure 3 c. We now capture both the maximum height and lateral extent of the TCE pool above CB4 as well as the invasion order quite well. Additionally, total TCE volume at breakthrough is now within 10% of the experimental value (see Table 3).

In comparison to experiment, while the simulated TCE fingers widen slightly by use of (5), they are still too narrow and their multiple and braided nature is not well represented. In GC&P, this second order viscous effect caused TCE finger saturation to increase well above that for CO_2 signifying an increase in the range of pore sizes that fill. At the 'front' where the relative permeability increases from zero, the influence of the randomness in the capillary pressure relative to the pressure drop due to viscous forces decreases as Q increases. Physically, the system cannot distinguish between blocks when their capillary pressures are within a certain range of each other and so the spread of R's selected should widen and local saturation increase. Thus in NP-MMIP, the range of P_t that is filled at each growth step should also increase as Q increases. This effect is similar to that emphasized in the work of Ewing and Berkowitz [1998] where they consider a random selection of a single pore within the range to be filled. Here we simply fill all the pores within the range that are accessible at a given growth step. In this sense, we consider viscous forces to

decrease the randomness imposed by capillary forces at the front. While a relationship between the range of P_t to be filled as a function of Q requires further study to properly parameterize, we include this effect roughly in the current model by simply filling a set number of blocks at the top of the sorted P_t list at each growth step.

A TCE order image is shown in Figure 3 d for a choice of blocks filled per growth step (60) that best matches the total volume of TCE at breakthrough. The braided nature of the growth structure as seen within each capillary barrier and within the coarse sand unit between CB3 and CB4 is reasonably well simulated. However, the multiple, independent finger formation seen in the experiment below CB4 is still not as strong. While two fingers form below the CB in the simulation, they do not remain independent, the one on the left stalling while the one on the right continued growth. This third order viscous effect may require full implementation of (4) or the imposition of an additional independancy criterion such as suggested by Ewing and Berkowitz [1998]. However, we note that multiple fingers also form in the CO_2 experiment due to pulsation even though viscous forces were negligible (see bottom of Figure 2a) and so thecause of independent fingers and thus their appropriate modeling, is as yet unclear.

3.5 Saturation fields for modified simulations:

Saturation fields for the experimental and final modified CO_2 and TCE NP-MMIP results are shown in Figure 4. As mentioned in GC&P, we have local error in the experimental saturation fields due to blurring around the edges of units and fingers. Because of this and the fact that we did not have a fully TCE saturated image to reduce the TCE data, the total volume in the experimental saturation image is under predicted by ~8% for CO_2 while that for TCE is over predicted by ~12%. Considering these errors, simulations and experiments appear very close. Average values of saturation within the center of pools where we have the least measurement error are within 1-2%. Saturations within CBs for TCE appear to be slightly under predicted, however, we have the most experimental error in these locations of unit transition. Additionally we note that use of an effective viscous effect such as (5) will slightly under emphasizes local viscous effects in the CB and thus should somewhat under predict the multiple and braided nature there while slightly over predicting it in the coarse layer. The simulated CO_2 and TCE saturation structures within the coarse sand between CB3 and CB4 is very similar to the experiment. This is also the case for the fingers below CB4.

Figures 5 and 6 show magnified and contrast enhanced images of the saturation fields at and below CB4. A series of simulations for increasing blocks per step is included for TCE in Figure 6. In all the images we see the beginnings of several fingers extending into the CB. For CO_2, both experiment and simulation show one finger to extend through the CB and grow below. For TCE, three fingers extend fully through the barrier in the experiment while two do so in the simulation. Multiple breaches occur for TCE in both simulations and experiment at all of the other CBs as well. Average finger widths below the CB4 are very close for the CO_2, while for the TCE, the simulated width at 60 blocks per step where the total volume at breakthrough is matched is closer to the combined width of all the fingers in the experiment. The finger width for 10 blocks per step better simulates the experimental width for an individual TCE finger. Obviously, if the IP algorithm is modified to allow independent fingers, Q for each would have to be determined and the appropriate number of blocks per step specified.

It is important to realize that working to simulate the finger structure better in macro-heterogeneous media such as considered here, is not very important by itself in the simulation of the total volume invaded. Note that if the second order viscous modification

that allows us to predict the multiple and braided finger structure in the TCE experiment is neglected, we are still within 10% on the invaded volume (see Figure 3 c and Table 3). It is clear that in order to reasonably predict the volume invaded, it is most important to properly predict pool heights, and it is in this context that fingers have a first order influence. Adequate recognition of the finger structure within a CB must be made to elevate the pool heights in the TCE experiments with a corresponding increase of ~200% in the total volume invaded.

Finally we note that in our current presentation, the simultaneous invasion of wetting and non-wetting fluid has not been considered and so pulsation is not simulated; we model a static invasion structure that is of maximum extent and saturation. Pulsation occurs throughout the CO_2 and parts of the TCE experiment, however, as we see here, it does not significantly influence the path in our particular macro-heterogeneous porous media nor the adequate prediction of the total invaded volume at breakthrough. For less intense heterogenieties, however, this may not be the case as is exemplified below CB4 where the single finger breaks into several with depth.

4. Summary and Conclusion

In the context of 'macro' modified invasion percolation (MMIP), we reconceptualize at the near pore (NP) scale and apply the model to simulate the non-wetting phase invasion experiments of GC&P conducted in macro-heterogeneous porous media. NP-MMIP shows the same characteristic alternation as found experimentally between gravity stabilized and destabilized invasion growth controlled by the presence of CBs. The breaching of these barriers and subsequent pore scale fingering of the non-wetting phase is represented extremely well by NP-MMIP. For the CO_2 experiment where viscous forces were negligible, slight modifications of the capillary properties (also suggested by the scale analysis of GC&P) were required to fully match the experimental pool heights, after which the total volume invaded matched experimental measurements. However, for the TCE experiment with a viscosity ~40 times that of CO_2, considerable discrepancies remain.

In order to consider situations where viscous forces are non-negligible, we redefined the total pore filling pressure to include viscous losses within the invading phase as well as its influence to decrease the randomness imposed by capillary forces at the front. Our simulations that include these viscous influences in an effective sense are shown to match experiments very well. However, full implementation of viscous forces using equation (4) is required for general model application. While our approach to incorporating viscous effects is based on experiments and the scale analyses presented in GC&P, it requires understanding of the role of viscous forces at the pore scale as the invasion process evolves. In particular, two general relationships must be built that model first the number of conducting backbone pores and second the indistinguishability between blocks at the front, each as a function of the flow rate. We show a good match to experiments when we can back calculate the appropriate values, however, currently these are little more than empirical 'knobs' that allow for calibration. Further research is required to theoretically and experimentally develop these general relationships.

Our current results another step further in the development of MMIP. Full evaluation of the influence of capillary, gravity, and viscous forces on length scales for finger diameter, and pool height at capillary barriers is now needed. The influence of simultaneous wetting and non-wetting fluid invasion that yields subsequent pulsation and independent fingers as well as the influence of sub-scale heterogeneities must also be considered. With these accomplished, the application of MMIP to field scale problems where sub-scale lengths are assembled to yield the non-wetting phase migration pathway directly may then be possible.

Acknowledgments

This research was partially supported by Sandia National Laboratory's Research and Development Program, the U.S. Department of Energy's Environmental Science Management Program and the U.S. Department of Energy's Basic Energy Science Geoscience Program. Will Peplinski reduced the experimental hetero-structure to the unit image used to create the realization for the R fields. The initial simulations in this paper were first presented by the senior author at the 1995 Fall American Geophysical Union meeting [Conrad et al., 1995] and conversations at that time with Toby Ewing, Brian Berkowitz, and Harvy Scher are gratefully acknowledged.

Sandia is a multiprogram laboratory operated by Sandia Corporation, a Lockheed Martin Company, for the United States Department of Energy under contract DE-AC04-94AL85000.

References

Conrad, S.H., R.J. Glass, W. Peplinski, L. Yarrington, and E.K. Webb, Nonaqueous phase liquid movement within heterogeneous porous media: Physical experiment and numerical simulation, *Eos Trans. AGU,* 76(46), Fall Meet. Suppl., 258, 1995.

Ewing, R.P, and B. Berkowitz, A generalized model for simulating initial migration of dense non-aqueous phase liquids, *Water Resources Research*, 34(4), 611-622, 1998.

Glass, R.J., S.H. Conrad, and W. Peplinski, Gravity destabilized non-wetting phase invasion in macro-heterogeneous porous media: Experimental observations of invasion dynamics and scale analysis, in review.

Glass, R.J., S.H. Conrad, and E.K. Webb, Percolation approaches to modeling immiscible fluid movement in subsurface systems, *Eos Trans. AGU,* 74(43), Fall Meet. Suppl., 278, 1993.

Glass, R.J., E.K. Webb and S.H. Conrad, An upscaled buoyant invasion percolation model for use in approaches to delineate subsurface DNAPL location, *AIChE Symposium Series*, 306(91), pp. 23-29, 1995.

Ioannidis, M.A., I. Chatzis, and F.A.L. Dullien, Macroscopic percolation model of immiscible displacement: Effects of buoyancy and spatial structure, *Water Resources Research*, 32(11), 3297-3310, 1996.

Kueper, B.H., and D.B. McWhorter, The use of macroscopic percolation theory to construct large-scale capillary pressure curves, *Water Resources Research*, 28:9:2425-2436, 1992.

Lenormand, R., C. Zarcone, Invasion percolation in an Etched Network: measurement of a fractal dimension, *Phys. Rev. Lett.* 54:2226-2229, 1985.

Reeves, P.C., and M.A. Celia, A functional relationship between capillary pressure, saturation and interfacial area as revealed by a pore-scale network model, *Water Resources Research*, 32(5), 2345-2358, 1996.

Wilkinson, D., and J.F. Willemsen, Invasion percolation: a new form of percolation theory, *J. Phys. A:Math. Gen.* 16:3365-3376, 1983.

Xu, B., Y.C. Yortos, and D. Salin, Invasion percolation with viscous forces, *Phys. Rev. E;* 57(1) 739-751, 1998.

Table 1: Sand properties*

Grain size	Sieve Size	k (cm^2)	mean grain (mm)	Porosity
Coarse	12-20	6.32E-06	1.087+/-0.001	0.35
Medium	30-40	1.20E-06	0.488+/-0.003	0.35
Fine	50-70	2.97E-07	0.259+/-0.001	0.36

*From GC&P

Table 2: Fluid properties*

Chemical	Density (g/ml)	interfacial tension (dyne/cm)	Viscosity (poise)
CO_2	0.196	71.40+/-0.85	1.48E-04
H_2O	0.998	NA	1.00E-02
TCE	1.464	26.90+/-0.63	5.76E-03

*From GC&P

Table 3: Invaded non-wetting volume at breakthrough

	notes	Volume (ml)*
CO_2		
Experiment	from GC&P	50.8
NP-MMIP	initial	68.7+/-0.6
NP-MMIP	modified R field (e.g., Figure 3a, 4b)	51.3+/0.5
TCE		
Experiment	from GC&P	73.1
NP-MMIP	initial	53.1+/-0.9
NP-MMIP	modified R field (e.g., Figure 3b)	31.9+/-0.3
NP-MMIP	modified R field, viscous 1 block/step (e.g., Figure 3c)	65.8+/0.8
NP-MMIP	modified R field, viscous 10 blocks/step	66.8+/0.6
NP-MMIP	modified R field, viscous 20 blocks/step	68.2+/0.6
NP-MMIP	modified R field, viscous 30 blocks/step	69.6+/0.6
NP-MMIP	modified R field, viscous 40 blocks/step	71.0+/0.5
NP-MMIP	modified R field, viscous 50 blocks/step	72.5+/0.5
NP-MMIP	modified R field, viscous 60 blocks/step (e.g., Figure 3d,4d)	73.8+/0.7

* STD associated with variation over 10 realizations

Figure Captions

Figure 1. Simulation of R field and unit drainage curves: a) Digital image of the heterogeneous sand pack used in the invasion experiments. In this image the coarse sand transmits the most light and hence is the lightest; the medium sand appears gray; and the fine sand appears dark. The injection port and four major capillary barriers (labeled CB1 through CB4) are identified. These capillary barriers occur where medium sand separates coarse sand units. b) Representative R field simulation using unit locations and CDFs built from drainage curves measured on each unit. c) Comparison of measured and simulated drainage curves for each unit (solid lines designate data and dashed simulations).

Figure 2. Experimental invasion order images and initial 3D NP-MMIP simulations: a) CO_2 experiment, b) CO_2 NP-MMIP simulation, c) TCE experiment, d) TCE NP-MMIP simulation. Colors represent first arrival filling order integrated across the thickness of the chamber or simulation network.

Figure 3. Modified 3D NP-MMIP simulations: a) CO_2 on scaled R field, b) TCE on scaled R field, c) TCE on scaled R field with first order viscous forces included, c) TCE on scaled R field with first and second order viscous forces included (60 blocks per step). Colors represent first arrival filling order integrated across the thickness of the chamber or simulation network.

Figure 4. 2D saturation fields at system breakthrough: a) CO_2 experiment, b) CO_2 NP-MMIP simulation on scaled R field, c) TCE experiment, d) TCE NP-MMIP simulation on scaled R field with first and second order viscous forces included (60 blocks per step). Colors represent non-wetting saturation averaged across the thickness of the chamber or simulation network, non-wetting residual saturation of 0.833 is noted on the color bar.

Figure 5. Magnified and contrast enhanced CO_2 saturation structures below CB4: a) CO_2 experiment, b) NP-MMIP simulation on the scaled R field. Saturation fields have been contrast enhanced to bring out the underlying pore scale nature of fingers in the 2D depth integrated fields. The box shows a representative CO_2 finger width of 0.7 cm.

Figure 6. Magnified and contrast enhanced TCE saturation structures below CB4: a) TCE experiment, and NP-MMIP simulations on the scaled R field with first and second order viscous effect with b) 1, c) 10, d) 20, e) 30, f) 40, g) 50, and h) 60 blocks per step. Saturation fields have been contrast enhanced to bring out the underlying pore scale nature of fingers in the 2D depth integrated fields. The box shows a representative TCE finger width of 1.2 cm.

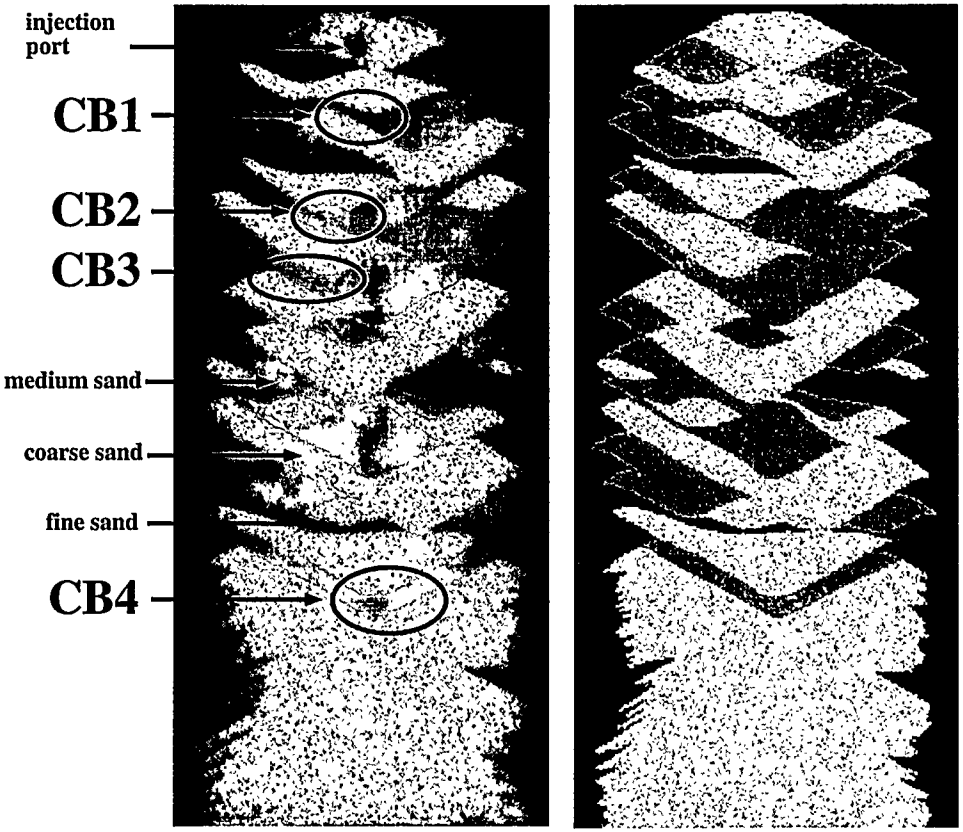

a) Experimental hetero-structure

b) Representative R field simulation

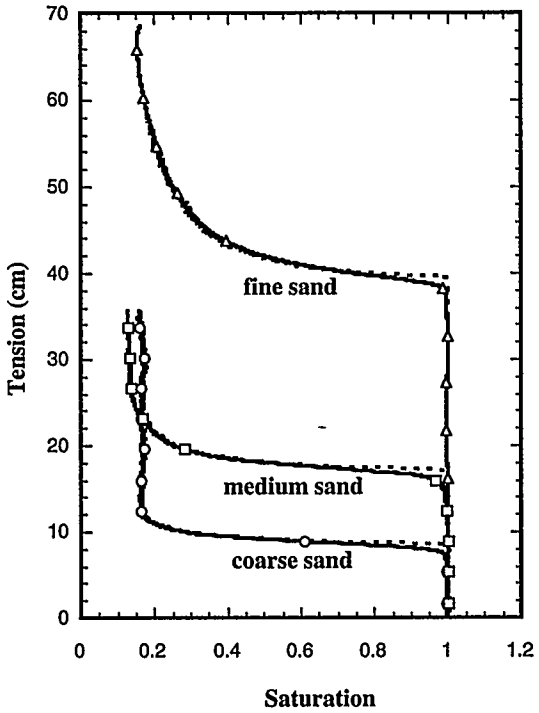

c) Drainage curve data and simulation

Figure 1

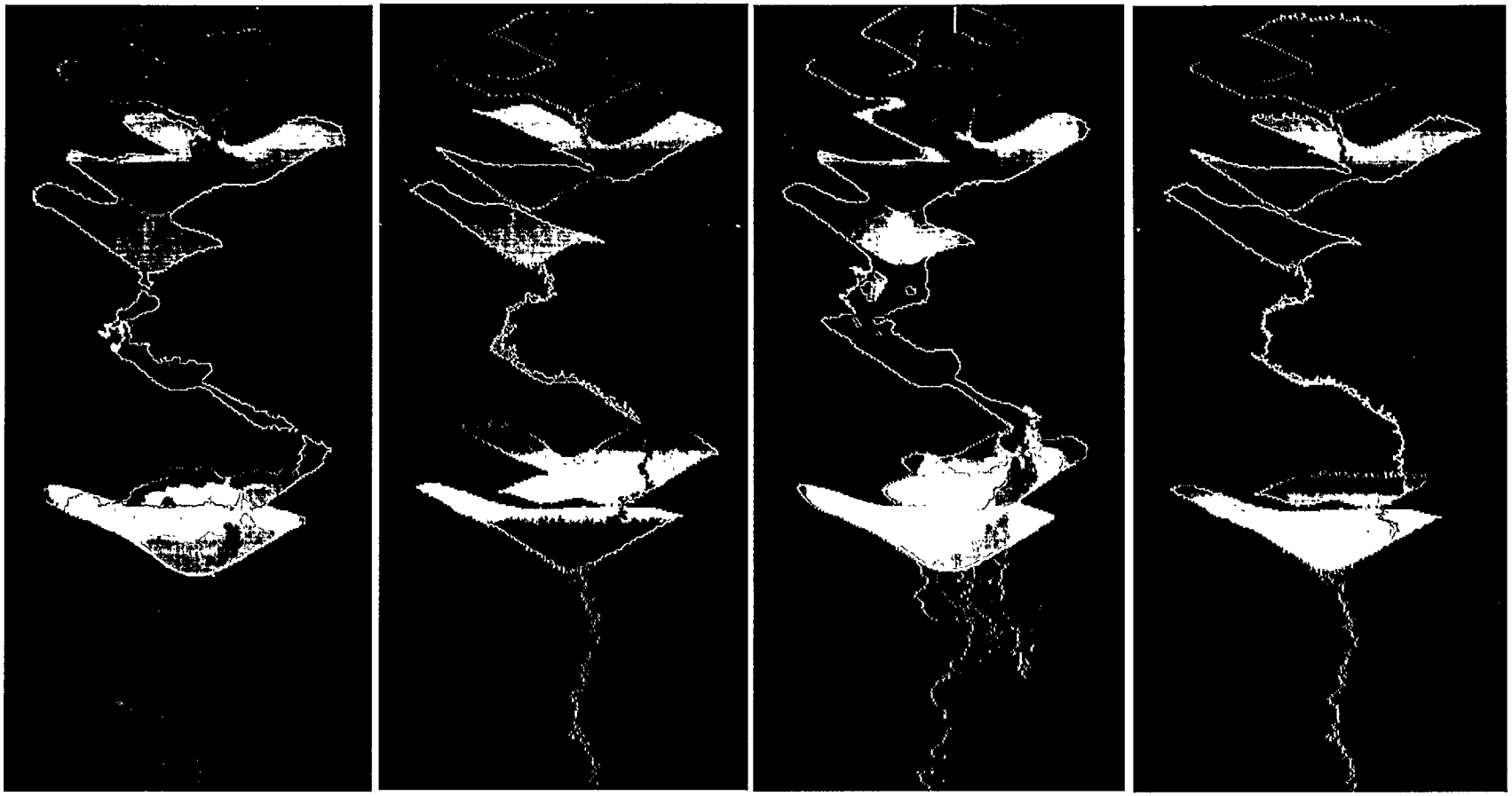

a) CO2 experimental b) CO2 initial simulation c) TCE experimental d) TCE initial simulation

filling order

Figure 2

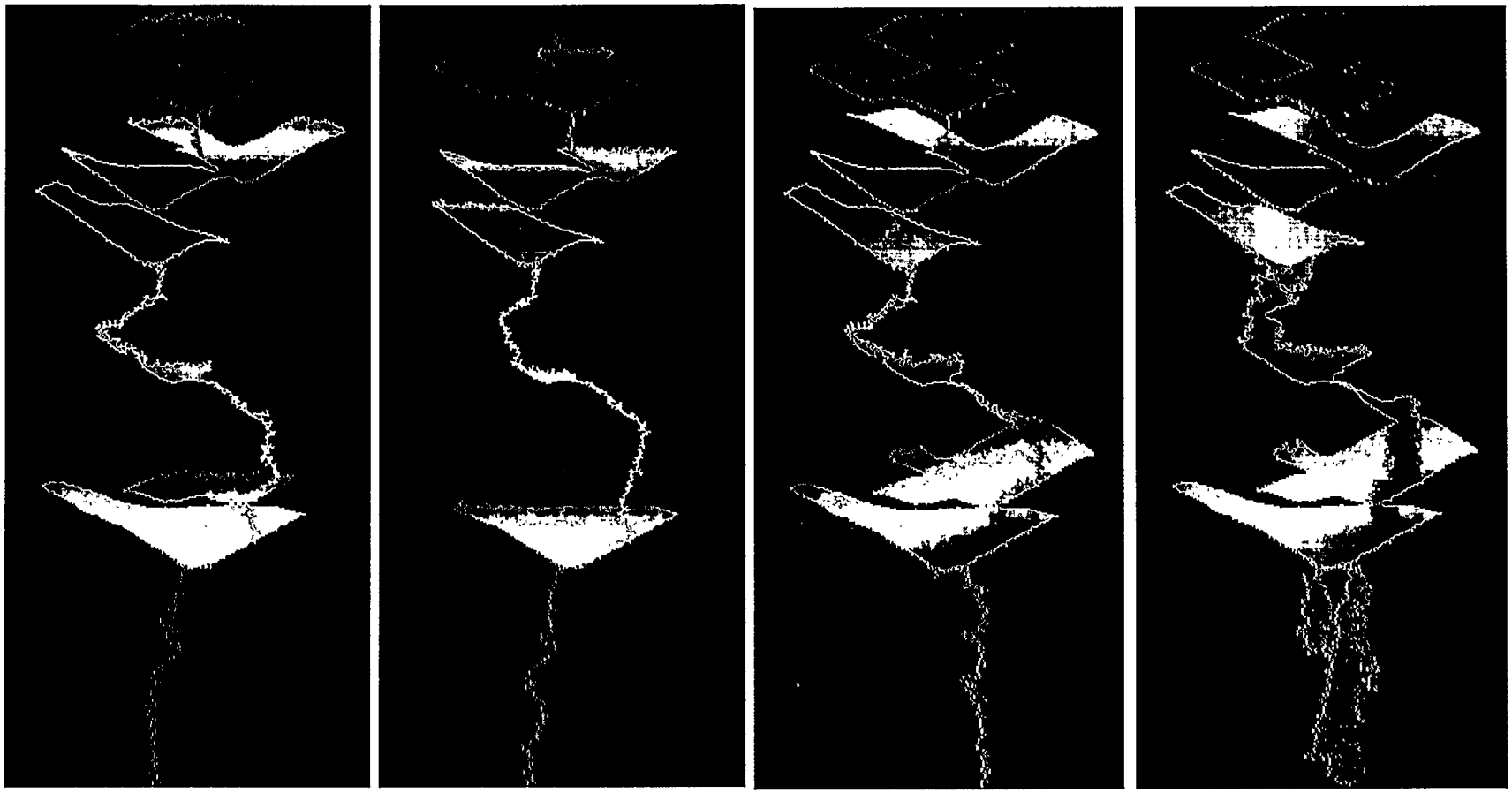

Figure 3

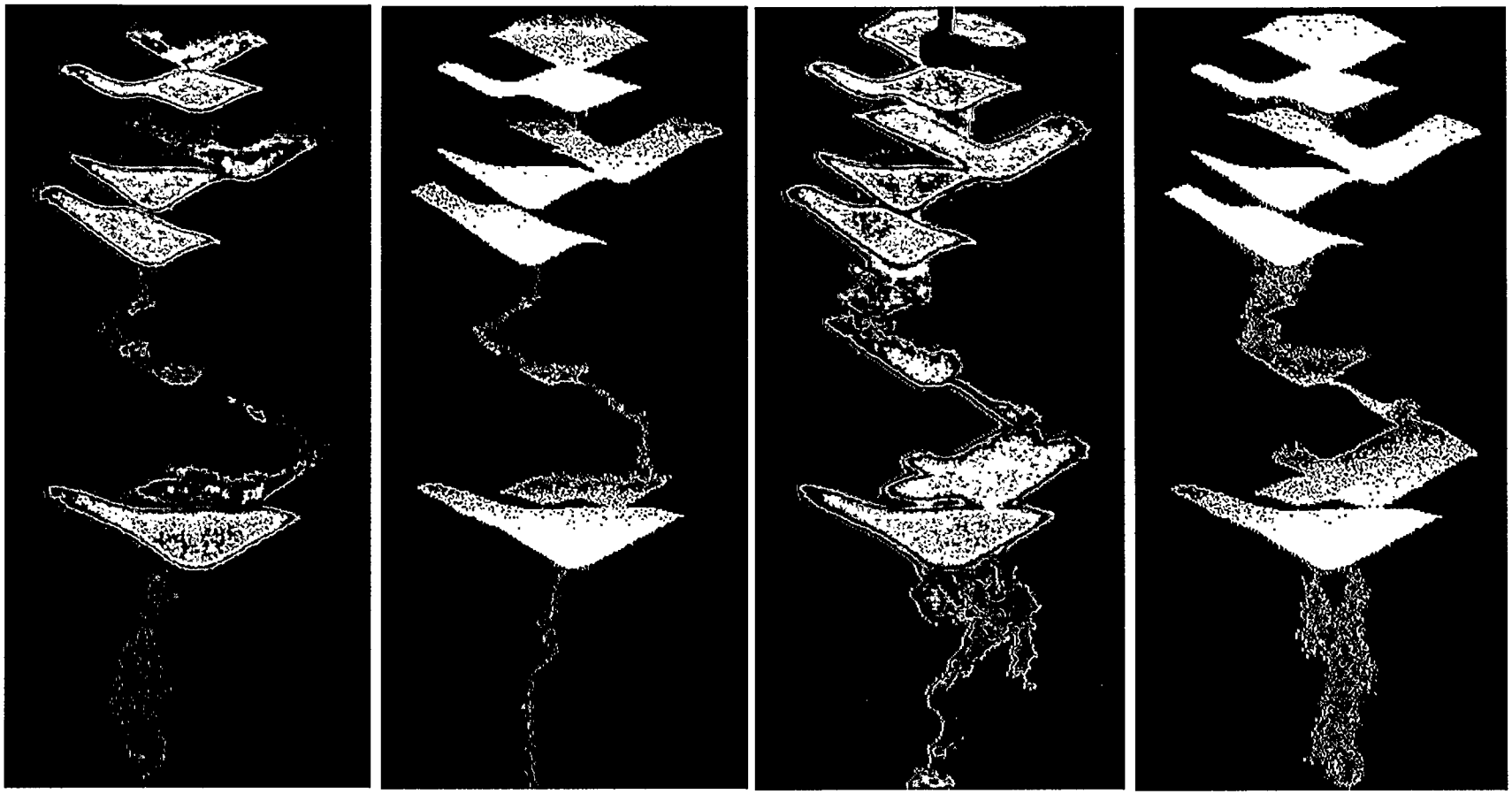

a) CO2 experimental b) CO2 final simulation c) TCE experimental d) TCE final simulation

Figure 4

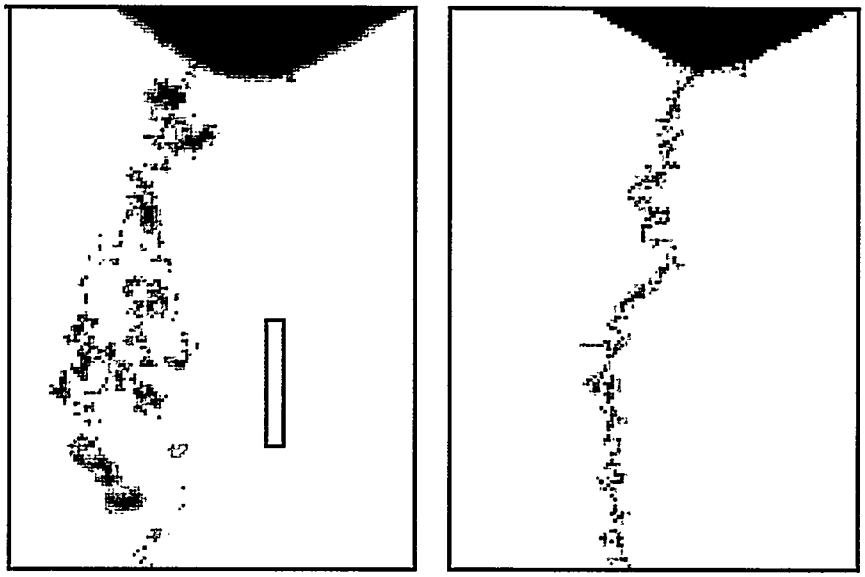

a) CO2 experiment b) NP-MMIP

Figure 5

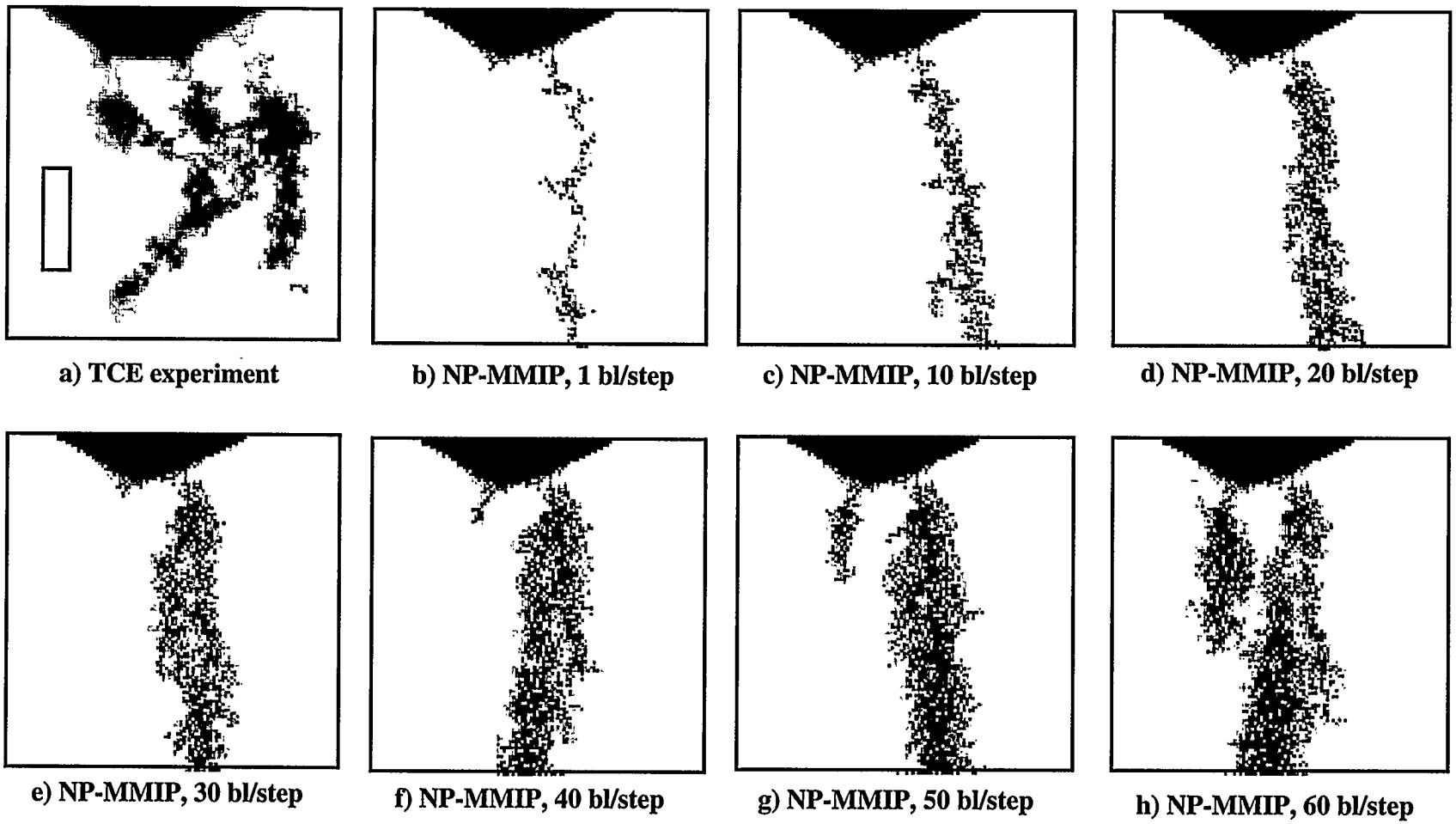

a) TCE experiment

b) NP-MMIP, 1 bl/step

c) NP-MMIP, 10 bl/step

d) NP-MMIP, 20 bl/step

e) NP-MMIP, 30 bl/step

f) NP-MMIP, 40 bl/step

g) NP-MMIP, 50 bl/step

h) NP-MMIP, 60 bl/step

Figure 6